

Additive Manufactured and Topology Optimized Permanent Magnet Spin-Rotator for Neutron Interferometry Applications

Wenzel Kersten¹, Laurids Brandl¹, Richard Wagner¹, Christian Huber^{2,3},
 Florian Bruckner^{2,3}, Yuji Hasegawa^{1,4}, Dieter Suess^{2,3}, and Stephan Sponar¹

¹Atominstitut, TU Wien, Stadionallee 2, 1020 Vienna, Austria

²Physics of Functional Materials, University of Vienna, 1090 Vienna, Austria

³Christian Doppler Laboratory for Advanced Magnetic Sensing and Materials, 1090 Vienna, Austria

⁴Department of Applied Physics, Hokkaido University, Kita-ku, Sapporo 060-8628, Japan

(Dated: November 1, 2018)

In neutron interferometric experiments using polarized neutrons coherent spin-rotation control is required. In this letter we present a new method for Larmor spin-rotation around an axis parallel to the outer guide field using topology optimized 3D printed magnets. The use of 3D printed magnets instead of magnetic coils avoids unwanted inductances and offers the advantage of no heat dissipation, which prevents potential loss in interferometric contrast due to temperature gradients in the interferometer. We use topology optimization to arrive at a design of the magnet geometry that is optimized for homogeneity of the magnetic action over the neutron beam profile and adjustability by varying the distance between the 3D printed magnets. We verify the performance in polarimetric and interferometric neutron experiments.

I. INTRODUCTION

Since its first demonstration in 1974, neutron interferometry [1, 2] has proven itself a powerful tool to study fundamental concepts of quantum mechanics. For instance the spin-superposition law [3, 4], gravitationally induced phases (Colella-Overhauser-Werner effect) [5] or the Sagnac effect [6] have been verified experimentally. Experiments challenging our views on reality include the Einstein-Podolsky-Rosen experiments, where a violation of Bell's inequality, assuming local hidden variables, can be measured. Using pairs of entangled photons [7–15] it can be shown that quantum mechanics is non-local, i.e., it cannot be reproduced by local realistic theories. Entanglement can not only be achieved for spatially separated particles but also between different degrees of freedom [16–20], e.g. path, spin and energy in the case of neutrons. This enables the experimental violation of Bell's inequality for non-contextual hidden variables using neutron interferometric setups [21, 22], giving proof that measurement outcomes are not predetermined and therefore depend on the experimental context [23, 24]. Not a statistical violation but a contradiction between quantum mechanics and local hidden variable theories was found by Greenberger, Horne and Zeilinger in 1989 for, at least, tripartite entanglement [25, 26], also feasible with neutrons [27]. More recently, a neutron optical approach for obtaining weak values [28], a new type of quantum variable introduced by Aharonov already three decades ago [29], has been realized. With this novel technique quantum paradoxes such as the Quantum Cheshire Cat [30] or a violation of the classical Pigeonhole effect [31] have been studied. In addition, a direct tomographic state reconstruction technique based on weak values, independent of the measurement strength, has been established [32]. Common to all these experiments is the requirement of high interference contrast and even more important, a high efficiency in spin manipulation

capacity, i.e., full control of the spin state.

II. 3D PRINTED SPIN-ROTATOR

The current setup to tests of fundamental phenomena in quantum mechanics Bell's inequality violation at the Institut Laue Langevin in Grenoble, France, is shown in Fig. 1. The Larmor spin-rotator has a Helmholtz coil geometry. It applies a local field in addition to the guide field in the z -direction, thereby locally changing the Larmor frequency, with which the spin precesses around the field in the xy -plane. The rotation angle is given by

$$\alpha(B_z) = \frac{2\mu_N}{\hbar} B_z \frac{l}{v} \quad (1)$$

where $\mu_N = -9.6623647 \times 10^{-27}$ J/T is the magnetic moment of a neutron, l is the length of the coil and v is the velocity of the neutrons. Since the local field and the guide field are parallel, the field transition can be adiabatic.

Such a Larmor spin-rotator must have a highly homogeneous field along the neutron beam path, because an inhomogeneous field would lead to a dephasing of the neutron and therefore to a loss in contrast of the interferogram. Another crucial point is the thermal stability of the setup. A change of temperature during the measurement leads to a loss in contrast, as phase drifts occur, e.g., a temperature change of 1 °C results in 1.92 rad phase shift [33]. For this reason the Helmholtz coil Larmor spin-rotator is water-cooled (Fig.1(b)), which complicates the setup of the experiment, because the temperature of the cooling water has to be optimized. In addition, the manufacture of waterproof boxes to hold the Helmholtz coils is tedious.

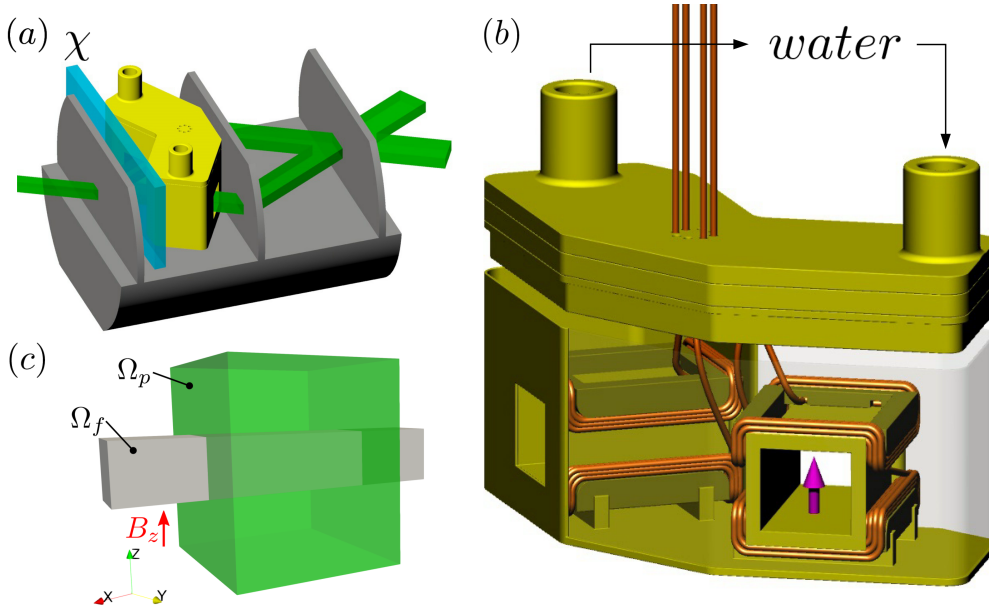


FIG. 1. Current neutron interferometric setup. (a) Placement of the box inside the neutron interferometer together with the phase shifter plate χ . (b) Schematic view of the water-cooled Larmor spin-rotator box with coils in Helmholtz geometry and magnetic field direction indicated in magenta. Also depicted are in and outlets for temperature-controlled cooling water. The box needs to be waterproof, which makes manufacture tedious. (c) Design and field domain for an optimized 3D printed permanent magnetic Larmor spin-rotator.

A. Requirements

To improve the design at hand, the actual condition should be examined in more detail. The neutron path is simplified by a field box Ω_f with a size of $7 \times 7 \times 40 \text{ mm}^3$ ($a \times a \times L$). To describe the influence of the magnetic field on the phase shift of the neutrons, the action Θ is defined as

$$\Theta = \frac{1}{a^2} \int_{\Omega_f} |B_z| d\mathbf{r}. \quad (2)$$

In order to rotate the neutron spin by an angle $\alpha = \pi$, an action of $\Theta = 35 \text{ mT} \cdot \text{mm}$ is necessary. The action of the Helmholtz coil geometry is calculated using the finite element method (FEM) tool Magnum.fe [34]. Fig. 2(a) shows the geometry as well as the field box with vectors of the magnetic field. The field shows an inhomogeneous behavior outside the coil. A calculation of the current I to reach an action of $\Theta = 35 \text{ mT} \cdot \text{mm}$ is plotted in Fig. 2(b). The relative error of the field homogeneity is plotted in 5(b). An optimized design should be found with the requirements, presented in the next subsection. The goal is to find an optimized permanent magnetic Larmor spin-rotator by the usage of the inverse stray field and topology optimization framework [35–37]. Following design parameters are given:

- Size of the field box Ω_f : $7 \times 7 \times 40 \text{ mm}^3$ ($a \times a \times L$).
- Maximum design volume Ω_p : $24 \times 24 \times 20 \text{ mm}^3$ ($a \times a \times L$).
- Action Θ of the external field: $\Theta = 35 \text{ mT} \cdot \text{mm}$.
- Θ is adjustable in the range of $\pm 5 \text{ mT} \cdot \text{mm}$.
- Homogeneous magnetic field density $\mathbf{B}(\mathbf{r})$ along z -axis: $\mathbf{B}(\mathbf{r}) = (0, 0, B_z)$.

A challenge for a permanent magnetic system is to make the action Θ adjustable. For the Helmholtz coil geometry, Θ is easily adjustable by the current through the coils. The easiest way to adjust Θ for a permanent magnetic setup is to change the distance between the neutron path (field box) and the magnets. To realize a homogeneous magnetic field density in the field box Ω_f , the functional for the minimization problem can be given by

$$J = \int_{\Omega_f} (|\nabla B_x|^2 + |\nabla B_y|^2 + |(\nabla B_z)_y|^2 + |(\nabla B_z)_z|^2) d\mathbf{r} \quad (3)$$

B. Two Candidate Designs

Two different initial designs are investigated to find a proper replacement of the Helmholtz coils. The first design is a modified Halbach cylinder [38]. To achieve a

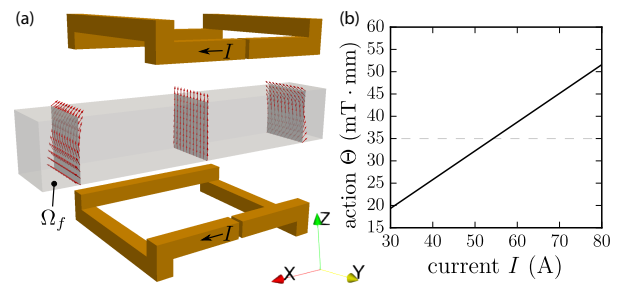


FIG. 2. Current driven Larmor spin-rotator. (a) Modified Helmholtz coil geometry with the field box Ω_f (equal to neutron beam size). Normalized magnetic field vectors in red. (b) Action Θ as a function of the current I through the Helmholtz coil.

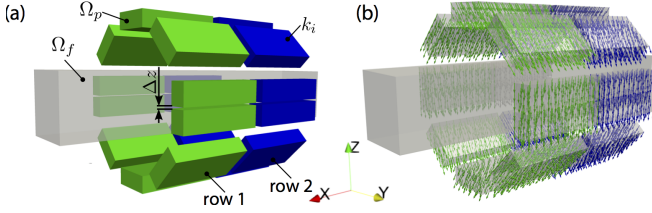


FIG. 3. Modified and optimized Halbach cylinder. (a) Initial layout with 20 segments. Remanence $|\mathbf{B}_r|$ is constant for each segment. Two rows should provide a homogeneous field outside of the magnets. (b) Result of the inverse stray field computation.

better field homogeneity outside the magnet, it is divided into two rows, which is schematically illustrated in Fig. 3. To adjust Θ , the design is split in the middle and the gap Δz between both halves is adjustable. In total 20 segments are used. Each permanent magnetic segment has a constant remanence $|\mathbf{B}_r|$, but the direction of \mathbf{B}_r is open and defines the optimization parameter for the inverse stray field optimization. Fig. 4(a) shows the initial design of the modified Halbach cylinder. Due to the fact that only the direction of the remanence is an optimization parameter, no regularization parameter is necessary. Fig. 3(b) shows the result of the inverse stray field simulation for an action of $\Theta = 35$ mT·mm. In general, the magnetization (remanence) vectors have the same direction as a standard Halbach cylinder, only the segments on the top and bottom of the field box show a deviating direction, to make the field in the field box more homogeneous.

The second investigated design is a topology optimized one. Fig. 4(a) shows the design domain Ω_p and the field box Ω_f where J of equation (3) should be minimized. To adjust Θ , the design consists of two halves, and the gap Δz is adjustable. The mesh of the design domain consist of 256,542 tetrahedral elements. No volume constraint is applied for the optimization. Fig. 4(b) shows the topology optimized version of a permanent magnetic Larmor spin-rotator.

Several numerical simulations are performed to find the optimal parameters of both designs. To adjust Θ in both directions, a gap of $\Delta z = 2.25$ mm is chosen. To get an action of $\Theta = 35$ mT·mm, a remanence of the permanent magnet of $B_r = 61$ mT for the topology optimized version and $B_r = 68$ mT for the Halbach design is necessary. How Δz and B_r influence Θ , is plotted in Fig. 5. There exists a linear correlation between action and gap size. The topology optimized design is less sensitive for changing Δz .

The homogeneity of $\mathbf{B}(\mathbf{r})$ in the field box Ω_f has a crucial impact on the performance. The relative error is defined as

$$\delta e = \frac{J}{\int_{\Omega_f} |\mathbf{B}|^2 d\mathbf{r}} \quad (4)$$

with the functional J of equation (3). Fig. 6(a) shows

the relative error δe as a function of the gap Δz . The topology optimized design has a much lower relative error compared to the Halbach cylinder design, and the dependency on the gap size is much lower as well. However, the main question is, if the optimized permanent magnetic design has a lower relative error, or a better performance as the current Helmholtz coil geometry. Fig. 6(b) shows a plot of the relative error as a function of the action for the current and the both optimized designs. For the current design, δe is independent of Θ . In the range of around of $\Theta = 30 - 40$ mT·mm the topology optimized version shows a better performance. This translates to a range of $\Delta z \simeq 1 - 3.5$ mm for the tunable gap distance.

C. Fabrication

For the manufacturing process of the permanent magnets, we use a conventional low-cost end-user 3D printer without any modifications [39] to print the topology optimized system. As a printing material the prefabricated compound material (Neofer® 25/60p) from Magnetfabrik Bonn GmbH is used to realize the setup. All four segments have the same shape. Fig. 4(c) shows a picture of the printed segments. After the printing process, the magnets must be magnetized. Compared to all previous applications, only a weak magnetic field is necessary. The segments must have exactly a remanence of $B_r = 61$ mT to generate an action of $\Theta = 35$ mT·mm for a gap of $\Delta z = 2.25$ mm. Magnetization of the segments are performed with an electromagnet with a maximum magnetic flux density inside the electromagnet of 1.9 T in permanent operation mode. A jig with the exact positions of the segments is 3D printed. The jig is inserted into the electromagnet and the external field is increased in small steps. After each step, the magnetic field density of the segments is measured by the 3D Hall probe. FEM simulation of the arrangement yields a field of $B_z = 1.18$ mT in the center for the desired action Θ . With this approach a good adjustment of the remanence B_r is possible.

After the magnetization procedure, the magnetic field between the segments is measured and compared with simulation results. Fig. 7(b) shows a volume scan between the segments and a line scan of B_z at $y = 0$ mm,

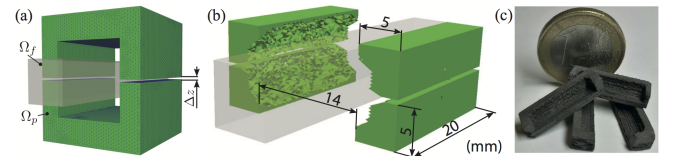


FIG. 4. Topology optimized design for the Larmor spin-rotator. (a) Design domain for the topology optimization approach. The action Θ is adjustable by the gap size Δz . (b) Topology after optimization. (c) Photo of the magnets printed with Neofer® 25/60p.

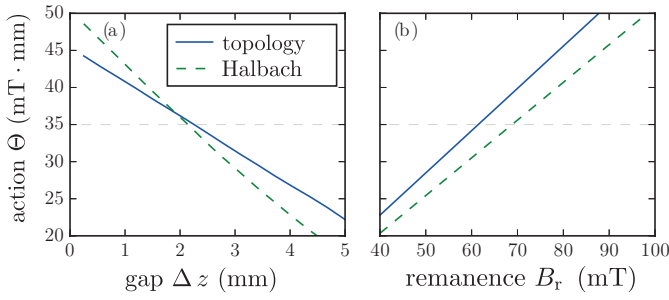


FIG. 5. Simulation results for both optimized designs. (a) Action Θ as a function of the gap Δz ($B_r = 61$ mT for the topology optimized design and $B_r = 68$ mT for the Halbach cylinder), and (b) as a function of the remanence B_r of the magnet (gap $\Delta z = 2$ mm).

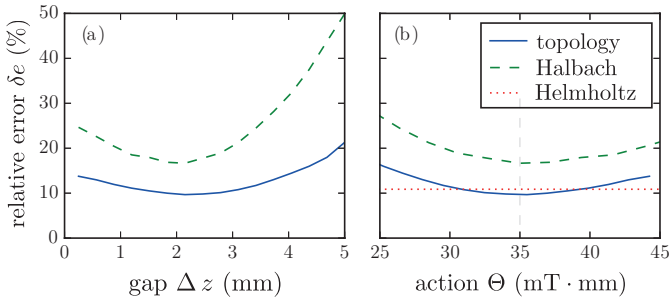


FIG. 6. Relative error for both optimized designs. (a) Relative error δe as a function of the gap Δz . (b) Relative error as a function of the action Θ for the optimized designs and for the current Helmholtz coil geometry.

$z = 0$ mm for the measured topology optimized version and the former Helmholtz coil geometry. Simulation results for $B_r = 61$ mT and measurements are in a good agreement. The vector field illustrates the homogeneity of the measurement and simulations, respectively.

III. PERFORMANCE IN NEUTRON OPTICAL EXPERIMENTS

A. Polarimeter experiment

The real performance of the 3D printed Larmor spin-rotator can be only tested with a neutron experiment. For this reason, interference measurements with neutrons are performed at the TRIGA MARK-II reactor at the Atominstut. Fig. 8 shows an illustration of the experimental setups. The gap Δz and therefore the action Θ can be adjusted by a 3D printed mounting system with counter-rotating threads. In the polarimeter experiment, depicted in Fig. 8(a), the first direct current spin turner DC1 rotates the spin of the neutrons in flight direction by an angle of $\pi/2$, then a cadmium aperture reduces the beam. After the aperture, the beam enters the 3D printed Larmor spin-rotator. The

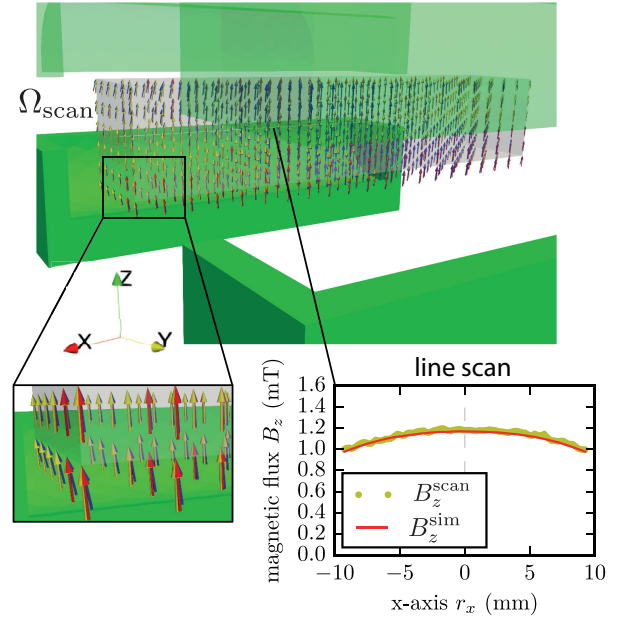


FIG. 7. Simulation and measurement of the magnetic field. Volume scan between the magnets for a gap of $\Delta z = 2.25$ mm. Magnetic vectors (blue: coil simulation, red: topology optimization simulation, yellow: measurement) illustrate the homogeneity of the field. Line scan of B_z at $y = 0$ mm, $z = 0$ mm.

intensity modulation is created by varying the position of DC2, which causes another $\pi/2$ spin-rotation around the x-axis. After DC2, the neutrons pass through a supermirror analyzer, transmitting only the $|+z\rangle$ -spin component into the detector.

Interference patterns for different Δz are plotted in Fig. 9(b). These are only test measurements with a small aperture opening of 3×5 mm². The reference measurement (black curve), from which the phase shifts are measured, is done without the Larmor spin-rotator. These measured phase shifts directly translate to the spin-rotation angle α . First measurements show a spin-rotation of $\alpha = \pi$ for a gap of $\Delta z = 2.25$ mm with the original remanence of $B_r = 61$ mT. This fits really well to the simulation for this action Θ . Another crucial parameter is the spin contrast C_S of the setup, which can be calculated from $C_S = \frac{I_0 - I_\pi}{I_0 + I_\pi}$, where I_π (I_0) is the intensity behind the spin analyzer after a π -flip (no flip). Here, a contrast of more than 95 % can be achieved for a gap of $\Delta z = 2.25$ mm.

However, the measurements showed such a promising linearity of the phase shift with Δz , that the 3D printed magnets were magnetized to a four times higher remanence of $B_r = 244$ mT, in order to have a wider tuning range of the spin-rotation angle α . Fig. 10 shows plots of α calculated from phase shifts of the interference patterns against Δz . These polarimetric measurements are carried out with an improved motorized adjustment mechanism for the gap distance and a wider aperture

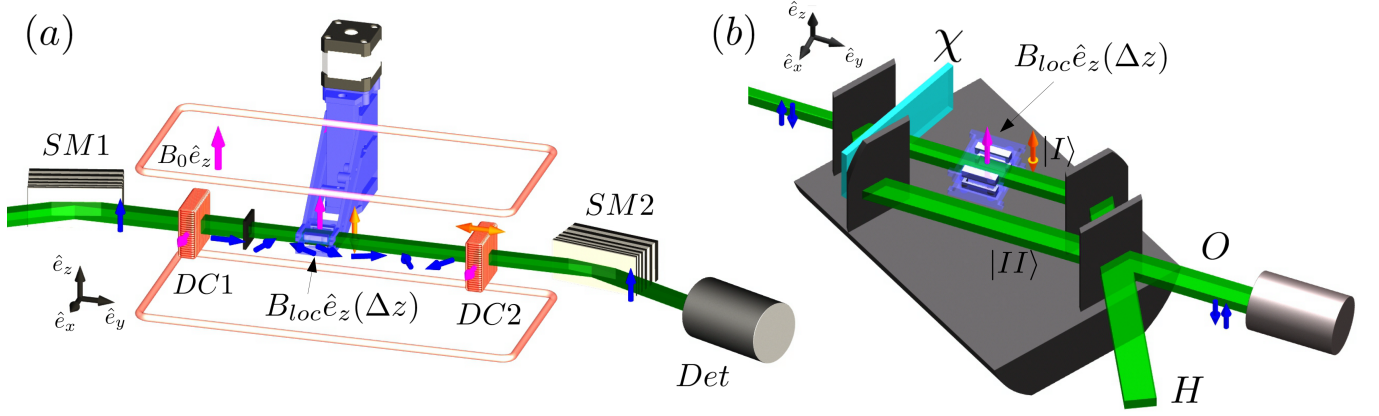


FIG. 8. 3D printed Larmor spin-rotator neutron interference experiments. (a) Illustration of the polarimetric setup. Polarized neutrons are flipped into (out of) the x-y-plane by direct current spin-rotators DC1 (DC2), where they rotate in the guide field B_0 due to Larmor precession. Arrows indicating spin directions (blue) and magnetic fields (magenta). The 3D printed magnets create an additional z-field $B_{loc}(\Delta z)$ that can be controlled by a motorized adjustment mechanism. The position of DC2 can be varied along the beam. After the spin direction is analyzed by the supermirror SM2, the neutrons are detected in a He-3 counter tube (Det). (b) Illustration of the interferometric setup. The monochromatized, unpolarized neutron beam is split in two parts, path $|I\rangle$ and $|II\rangle$. Their relative phase can be adjusted by rotating the phase shifter plate (χ). The 3D printed magnets with variable Δz are placed in path I . At the last interferometer plate, the two paths recombine and neutrons in the O beam pass on into the detector.

of $7 \times 7 \text{ mm}^2$. They show a good linearity of the spin-rotation angle against the gap size.

B. Interferometer experiment

As an example of the performance of the newly fabricated spin-rotators at their intended application inside a perfect crystal neutron interferometer, measurements are carried out at the Atominstut. The experiment is comparable to the first demonstration of the 4π -spinor symmetry of neutrons [40], its setup is depicted in Fig. 8(b). The unpolarized neutron beam with a cross section of $10 \times 10 \text{ mm}^2$ is split in path $|I\rangle$ and $|II\rangle$ after the first interferometer plate. The phase shifter plate can be rotated in order to create a phase difference

χ between the two paths. The 3D printed Larmor spin-rotator with variable Δz is placed in path I . At the last interferometer plate, the two paths are recombined and leave the interferometer in two separate beams, the O beam in the forward direction and the reflected H beam. Only the O beam has the same number of reflections and transmissions, and therefore is able to show maximum interferometric contrast C , when the phase shift χ is varied. The O beam intensity of an empty interferometer as a function of χ can be written as [2]

$$I_O(\chi) = |\Psi_0|^2(1 + C \cos \chi). \quad (5)$$

Here, C is a parameter and depends on the interferometer used, temperature gradients, vibrations, etc. The density matrix of an unpolarized neutron in the

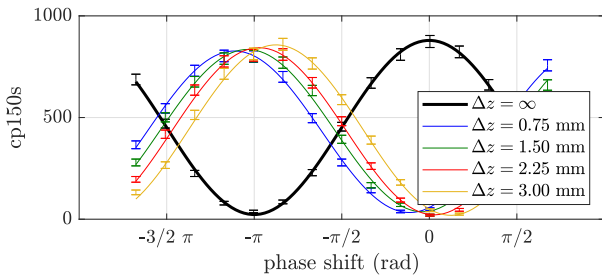


FIG. 9. Polarimetric test measurements of the spin-rotation angle caused by the 3D printed magnets with remanence $B_r = 61 \text{ mT}$. Interference patterns for different Δz attained by translating DC2 along the beam.

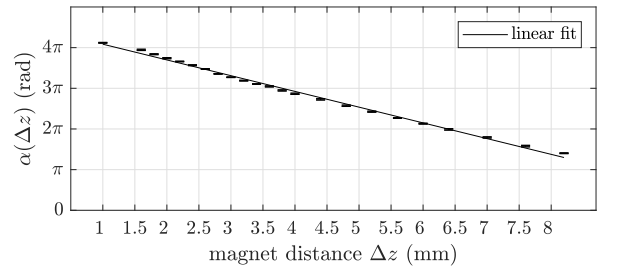


FIG. 10. Later polarimetric measurements with four times higher remanence $B_r = 244 \text{ mT}$. Spin-rotation angle α of the measured interference patterns calculated from sine fits against magnet distance Δz . The reference measurement is $\Delta z = \infty$, i.e. magnets taken out of the beam.

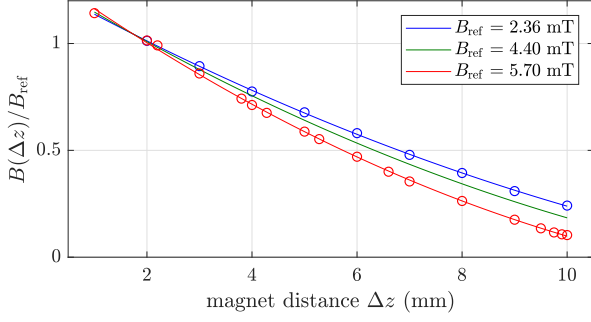


FIG. 11. Plot of the magnetic field at the center of the 3D printed Larmor-spin rotator, normalized by the value B_{ref} measured at $\Delta z = 2.25$ mm. For $B_{\text{ref}} = 2.36$ mT and $B_{\text{ref}} = 5.70$ mT the magnetic field has been measured using a Hall probe and fitted with a quadratic polynomial. The curve for $B_{\text{ref}} = 4.40$ mT is interpolated using these fits.

interferometer, assuming perfect contrast $C = 1$, can be written as the direct product

$$\rho = \frac{1}{2} |\psi_i\rangle\langle\psi_i| \otimes \frac{1}{2} (|\uparrow\rangle\langle\uparrow| + |\downarrow\rangle\langle\downarrow|), \quad (6)$$

where the first term in the product is the path state $|\psi_i\rangle = \frac{1}{\sqrt{2}}(|I\rangle + e^{i\chi}|II\rangle)$, which depends on the phase shift χ , and the second term is the maximally mixed spin state. The interaction with the local magnetic field in path I can be modeled as

$$U_{\text{int}}(\alpha) = |I\rangle\langle I| \otimes e^{i\frac{\alpha}{2}\sigma_z} + |II\rangle\langle II| \otimes \mathbb{1}, \quad (7)$$

where α depends on $B_{\text{loc}}(\Delta z)$ and is given by equation (1), when B is homogeneous. At the last interferometer plate, the projector $P_f = |\psi_f\rangle\langle\psi_f| \otimes \mathbb{1}$ acts on the path state and projects it onto the state $|\psi_f\rangle = \frac{1}{\sqrt{2}}(|I\rangle + |II\rangle)$. Therefore, the intensity at the O detector is given by

$$I_O(\chi, \alpha(\Delta z)) \propto \frac{1}{C} \text{Tr}(P_f U_{\text{int}} \rho U_{\text{int}}^\dagger P_f^\dagger) + \frac{C-1}{C} \quad (8)$$

$$= \frac{1}{2} \left(1 + C \cos\left(\frac{\alpha}{2}\right) \cos(\chi) \right),$$

where the empirical prefactor C has been reintroduced in front of the interference term. The interferometric contrast $C \cos(\alpha/2)$ is reduced to zero for odd multiples of the spin rotation angle $\alpha = \pi$, i.e., when the spin states in the two paths are orthogonal. At $\alpha = 2\pi$ the interferogram exhibits a phase shift of π compared to $\alpha = 0$, i.e. magnets removed. Only at $\alpha = 4\pi$ the interferogram has returned to its initial contrast and phase, which shows the 4π -symmetry of the neutron as a spin-1/2 particle.

In order to experimentally demonstrate this 4π -symmetry in a neutron interferometer experiment, three different magnetization strengths of the 3D printed Larmor spin-rotator are used, each identified by the magnetic field strength B_{ref} measured in the center point at

$\Delta z = 2.25$ mm. Measurements of the dependence of the magnetic field on the distance Δz are plotted in Fig. 11. For distances upwards of 8 mm, the magnetic field ceases to be linear. Nevertheless, interferograms are recorded for Δz up to 10 mm and plotted against the magnetic field calculated from fits with a quadratic polynomial. In Fig. 12 the results of the interferometric measurements are depicted, which clearly reproduce the 4π -symmetry in the experiment.

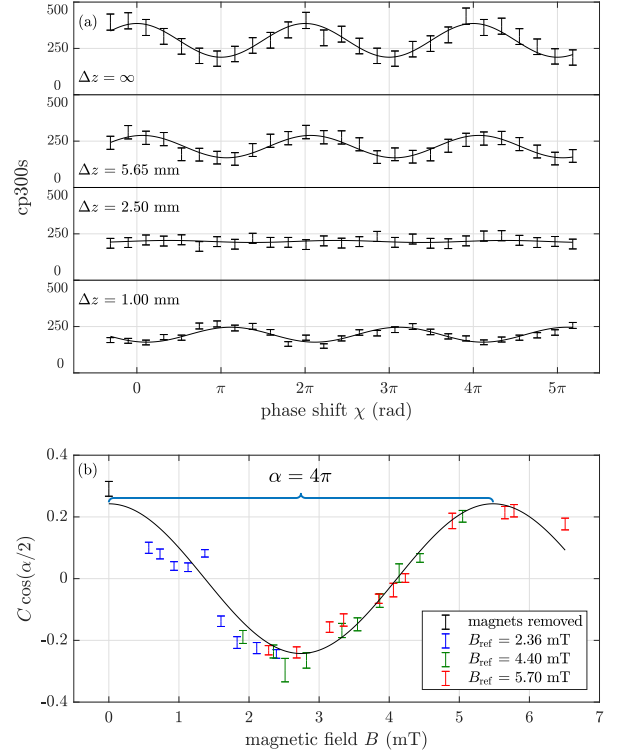


FIG. 12. Interferometric measurement results. (a) Typical interferograms for different values of Δz . The curves shown have been measured for $B_{\text{ref}} = 4.40$ mT. (b) Plot of $C \cos(\alpha/2)$ extracted from fits to the recorded interferograms against the magnetic field at the center of the 3D printed Larmor spin-rotator. Different data points have been measured using different magnetization strengths.

IV. DISCUSSION AND OUTLOOK

The combination of 3D printing and topology optimization using FEM methods offers new possibilities for tackling design problems, e.g. restrictions in available space to implement physical interactions. The design goal of this work, a Larmor spin-rotator consisting of a region of homogeneous magnetic field density, which is also tunable in magnitude, is met by a setup of four segments which are located to the sides of the field box. Tunability of the magnetic field strength is

realized by introducing a variable gap between the top and bottom half of the spin-rotator. The new method can be used in applications, where electromagnetic coils are unfavorable, e.g., due to heat dissipation or undesired inductances. Future developments could include different field configurations. One example is a spin-rotation field, which is perpendicular to the guide field and a non-adiabatic field transition is required. Another possible field configuration is that of a wiggler, which consists of stacked regions of anti-parallel magnetic fields along the beam-path. The spatial variation of the magnetic fields in the wiggler leads to resonant Rabi-flops of the spin, similar to the working principle of a resonant-frequency spin-flipper, where the variation happens in the time-domain. Using such devices, it is also possible to shape the beam-profile in momentum space. The new Larmor spin-rotator design developed in this work can be seen as a first step toward an implementation of custom magnetic field shaping using 3D printed permanent magnets in neutron optics.

V. CONCLUSION

We have developed a new method for coherent Larmor spin-rotation control using topology optimized 3D printed magnets for applications in neutron interferometer experiments, where the rotation axis is parallel to the outer guide field. The magnetic action can be adjusted linearly by varying the distance between the magnets. We have showed that spin-rotation angles of more than 4π are possible, depending on the initial magnetization strength. Measurements are in good agreement with simulations and showed a spin contrast of more than 95%, comparable to older methods using Helmholtz coils. The advantages of this new method are that unwanted inductances are avoided, and that no heat is dissipated by current carrying wires, which prevents a reduction in interferometric contrast due to temperature gradients or would make water cooling necessary.

-
- [1] H. Rauch, W. Treimer, and U. Bonse, *Phys. Lett. A* **47**, 369 (1974).
 - [2] H. Rauch and S. A. Werner, *Neutron Interferometry* (Clarendon Press, Oxford, 2000).
 - [3] J. Summhammer, G. Badurek, H. Rauch, U. Kischko, and A. Zeilinger, *Phys. Rev. A* **27**, 2523 (1983).
 - [4] G. Badurek, H. Rauch, and J. Summhammer, *Phys. Rev. Lett.* **51**, 1015 (1983).
 - [5] R. Colella, A. W. Overhauser, and S. A. Werner, *Phys. Rev. Lett.* **34**, 1472 (1975).
 - [6] S. A. Werner, J. L. Staudenmann, and R. Colella, *Phys. Rev. Lett.* **42**, 1103 (1979).
 - [7] R. A. Bertlmann and A. Zeilinger, *Quantum [Un]speakeables, from Bell to Quantum Information*, edited by R. A. Bertlmann and A. Zeilinger, Springer Verlag, Heidelberg (2002).
 - [8] S. J. Freedman and J. F. Clauser, *Phys. Rev. Lett.* **28**, 938 (1972).
 - [9] A. Aspect, P. Grangier, and G. Roger, *Phys. Rev. Lett.* **49**, 91 (1982).
 - [10] P. G. Kwiat, K. Mattle, H. Weinfurter, A. Zeilinger, A. V. Sergienko, and Y. Shih, *Phys. Rev. Lett.* **75**, 4337 (1995).
 - [11] G. Weihs, T. Jennewein, C. Simon, H. Weinfurter, and A. Zeilinger, *Phys. Rev. Lett.* **81**, 5039 (1998).
 - [12] W. Tittel, J. Brendel, H. Zbinden, and N. Gisin, *Phys. Rev. Lett.* **81**, 3563 (1998).
 - [13] M. A. Rowe, D. Kielpinski, V. Meyer, C. A. Sackett, W. Itano, C. Monroe, and D. J. Wineland, *Nature (London)* **409**, 791 (2001).
 - [14] M. Giustina, M. A. M. Versteegh, S. Wengerowsky, J. Handsteiner, A. Hochrainer, K. Phelan, F. Steinlechner, J. Kofler, J.-A. Larsson, C. Abellán, W. Amaya, V. Pruneri, M. W. Mitchell, J. Beyer, T. Gerrits, A. E. Lita, L. K. Shalm, S. W. Nam, T. Scheidl, R. Ursin, B. Wittmann, and A. Zeilinger, *Phys. Rev. Lett.* **115**, 250401 (2015).
 - [15] B. Hensen, H. Bernien, A. E. Dreau, A. Reiserer, N. Kalb, M. S. Blok, J. Ruitenberg, R. F. L. Vermeulen, R. N. Schouten, C. Abellan, W. Amaya, V. Pruneri, M. W. Mitchell, M. Markham, D. J. Twitchen, D. Elkouss, S. Wehner, and R. H. T. H. Taminiau, *Nature (London)* **526**, 682 (2015).
 - [16] D. L. Moehring, M. J. Madsen, B. B. Blinov, and C. Monroe, *Phys. Rev. Lett.* **93**, 090410 (2004).
 - [17] D. N. Matsukevich, P. Maunz, D. L. Moehring, S. Olmschenk, and C. Monroe, *Phys. Rev. Lett.* **100**, 150404 (2008).
 - [18] Y. Hasegawa, R. Loidl, G. Badurek, M. Baron, and H. Rauch, *Nature* **425**, 45 (2003).
 - [19] H. Sakai, T. Saito, T. Ikeda, K. Itoh, T. Kawabata, H. Kuboki, Y. Maeda, N. Matsui, C. Rangacharyulu, M. Sasano, Y. Satou, K. Sekiguchi, K. Suda, A. Tamii, T. Uesaka, and K. Yako, *Phys. Rev. Lett.* **97**, 150405 (2006).
 - [20] H. Geppert-Kleinrath, T. Denkmayr, S. Sponar, H. Lemmel, T. Jenke, and Y. Hasegawa, *Phys. Rev. A* **97**, 052111 (2018).
 - [21] Y. Hasegawa, R. Loidl, G. Badurek, M. Baron, and H. Rauch, *Phys. Rev. Lett.* **97**, 230401 (2006).
 - [22] H. Bartosik, J. Klepp, C. Schmitzer, S. Sponar, A. Cabello, H. Rauch, and Y. Hasegawa, *Phys. Rev. Lett.* **103**, 040403 (2009).
 - [23] J. S. Bell, *Rev. Mod. Phys.* **38**, 447 (1966).
 - [24] N. D. Mermin, *Rev. Mod. Phys.* **65**, 803 (1993).
 - [25] D. M. Greenberger, M. A. Horne, and A. Zeilinger, in *Bell's Theorem, Quantum Theory, and Concepts of the Universe*, edited by M. Kafatos (Kluwer Academics, Dordrecht, The Netherlands, 1989) pp. 73–76.
 - [26] D. M. Greenberger, A. Shimony, M. A. Horne, and A. Zeilinger, *Am. J. Phys.* **58**, 1131 (1990).
 - [27] Y. Hasegawa, R. Loidl, G. Badurek, K. Durstberger-Rennhofer, S. Sponar, and H. Rauch, *Phys. Rev. A* **81**, 032121 (2010).
 - [28] S. Sponar, T. Denkmayr, H. Geppert, H. Lemmel, A. Matzkin, J. Tollaksen, and Y. Hasegawa, *Phys. Rev. A* **92**, 062121 (2015).

- [29] Y. Aharonov, D. Z. Albert, and L. Vaidman, *Phys. Rev. Lett.* **60**, 1351 (1988).
- [30] T. Denkmayr, H. Geppert, S. Sponar, H. Lemmel, A. Matzkin, J. Tollaksen, and Y. Hasegawa, *Nat. Commun.* **5**, 4492 (2014).
- [31] M. Waegell, T. Denkmayr, H. Geppert, D. Ebner, T. Jenke, Y. Hasegawa, S. Sponar, J. Dressel, and J. Tollaksen, *Phys. Rev. A* **96**, 052131 (2017).
- [32] T. Denkmayr, H. Geppert, H. Lemmel, M. Waegell, J. Dressel, Y. Hasegawa, and S. Sponar, *Phys. Rev. Lett.* **118**, 010402 (2017).
- [33] H. Geppert, T. Denkmayr, S. Sponar, H. Lemmel, and Y. Hasegawa, *Nuclear Instruments and Methods in Physics Research Section A: Accelerators, Spectrometers, Detectors and Associated Equipment* **763**, 417 (2014).
- [34] C. Abert, L. Exl, F. Bruckner, A. Drews, and D. Suess, *Journal of Magnetism and Magnetic Materials* **345**, 29 (2013).
- [35] F. Bruckner, C. Abert, G. Wautischer, C. Huber, C. Vogler, M. Hinze, and D. Suess, *Scientific reports* **7**, 40816 (2017).
- [36] C. Huber, C. Abert, F. Bruckner, M. Groenefeld, S. Schuschnigg, I. Teliban, C. Vogler, G. Wautischer, R. Windl, and D. Suess, *Scientific reports* **7**, 9419 (2017).
- [37] C. Huber, C. Abert, F. Bruckner, C. Pfaff, J. Kriwet, M. Groenefeld, I. Teliban, C. Vogler, and D. Suess, *Journal of Applied Physics* **122**, 053904 (2017).
- [38] R. Bjørk, C. R. H. Bahl, A. Smith, and N. Pryds, *Journal of Magnetism and Magnetic Materials* **322**, 3664 (2010).
- [39] C. Huber, C. Abert, F. Bruckner, M. Groenefeld, O. Muthsam, S. Schuschnigg, K. Sirak, R. Thanhoffer, I. Teliban, C. Vogler, *et al.*, *Applied Physics Letters* **109**, 162401 (2016).
- [40] H. Rauch, A. Zeilinger, G. Badurek, A. Wilfing, W. Bauspiess, and U. Bonse, *Physics Letters A* **54**, 425 (1975).